J. Fluid Mech. (2011), *vol.* 686, *pp.* 5–25. © Cambridge University Press 2011
doi:10.1017/jfm.2011.272

Dense suspensions in rotating-rod flows: normal stresses and particle migration

François Boyer†, Olivier Pouliquen and Élisabeth Guazzelli

IUSTI-CNRS UMR 6596, Polytech-Marseille, Aix-Marseille Université (U1), Technopôle de Château-Gombert, 13453 Marseille cedex 13, France

(Received 17 September 2010; revised 16 May 2011; accepted 20 June 2011; first published online 30 August 2011)

Normal stress differences are measured in dense suspensions of neutrally buoyant non-Brownian spheres dispersed in a Newtonian fluid. Rotating-rod rheometry is used to characterize the suspension normal stresses which are responsible for a rod-dipping phenomenon. These normal stress differences are seen to strongly increase above a volume fraction of approximately 22 %. During the course of the experiments, a new time-dependent behaviour is also observed: the dip is filled with increasing times. This time evolution is found to be related to particle migration from regions of high shear rate to regions of low shear rate. The behaviour is compared with the predictions of a suspension balance model in which the particle migration flux is related to the normal stresses of the suspension.

Key words: particle/fluid flow, rheology, suspensions

1. Introduction

Suspensions of solid particles dispersed in a liquid are complex fluids that have been studied extensively for over a century. The main reason for this continuous interest is their considerable relevance for a wide range of industrial applications. Common examples include fresh concrete, cosmetics, paints and slurry transport to name a few. Suspensions are also involved in biological systems such as blood cells in plasma, and in natural phenomena such as mud flows and landslides. The rheology of suspensions presents a large variety of flowing behaviours (e.g. shear thinning, shear thickening and thixotropy) depending on the microstructure of the materials, the nature of the interactions involved and the properties of the carrier liquid. We only consider here neutrally buoyant suspensions of non-Brownian hard spherical particles in a Newtonian liquid. In these systems, hydrodynamic and contact forces are the only interactions that can contribute to the mechanics of the suspension. Despite this apparent simplicity and the large number of experimental, numerical and theoretical investigations, the rheology of suspensions remains an active research field as no unifying view has been proposed yet.

The dilute and semidilute regimes are well understood since the pioneering works of Einstein (1905) and Batchelor & Green (1972). In the past three decades, consideration has focused on concentrated (or dense) suspensions, defined as the regime where the average separation distance between particles is smaller than the

† Email address for correspondence: francois.boyer@polytech.univ-mrs.fr

https://doi.org/10.1017/jfm.2011.272 Published online by Cambridge University Press

particle size (see e.g. Stickel & Powell 2005). In this regime, multiple-body and short-range interactions give rise to non-Newtonian effects that can lead to misinterpretations of classical rheological measurements as pointed out by Ovarlez, Bertrand & Rodts (2006). As the microstructure of the suspension is a crucial feature of such dense systems and remains poorly understood, constitutive equations relating stress to the strain rate are not generally known (see e.g. Morris 2009).

As suggested by dimensional analysis (Krieger 1963, 1972) and confirmed by experimental observations and numerical simulations, dense suspensions of neutrally buoyant non-Brownian hard spheres are found to exhibit a Newtonian relation between the stress and shear rate allowing a suspension viscosity to be defined. Numerous authors have reported experimental data of relative suspension viscosity at different particle concentrations. As expected intuitively, the suspension viscosity increases with the concentration and, in the dense regime, a divergence of viscosity is observed at a maximum packing fraction ϕ_m. This behaviour can be captured by empirical functions which are kept consistent with the dilute predictions. Owing to large scatter in the data, there is no general agreement on the value of ϕ_m (which is seen to range from 0.58 to 0.68) or on the form of the viscosity curve close to the divergence.

While they play a essential role in the suspension rheology, normal stresses have been less documented. Zarraga, Hill & Leighton (2000) have performed a comprehensive study of normal stresses and have shown that the normal stress differences N_1 and N_2 are both negative and proportional to the shear stress (or the shear rate) modulus with $|N_1| < |N_2|$. Singh & Nott (2003) have measured both normal stress differences in cylindrical Couette and parallel-plate geometries with an experimental technique designed to increase the signal-to-noise ratio. Their results are in qualitative agreement with those of Zarraga *et al.* (2000) but there can be a factor of two difference between these two sets of data, which to the best of the authors' knowledge are the only measurements of normal stresses available in the literature. In addition, no experimental data are reported below a volume fraction of 0.3. Stokesian dynamics simulations have also been used to investigate the dense suspension rheology and microstructure (Singh & Nott 2000; Sierou & Brady 2002). Despite the limited number of particles, the suspension viscosity as well as the normal stress differences are qualitatively found in agreement with the experimental data. Interestingly, Sierou & Brady (2002) have suggested that frictional particle contact can have a critical effect on the magnitude of normal stress differences. This may explain the discrepancy found between numerical and experimental results. Analytic calculations can only be made in the dilute limit (see e.g. Nir & Acrivos 1973). More recently, Wilson (2005) has computed the second normal stress difference arising from a pair of interactions in the presence of particle roughness.

The objective of the present paper is to report on measurements of normal stress differences in dense suspensions of neutrally buoyant non-Brownian spheres. Following Zarraga *et al.* (2000), rotating-rod rheometry was used to characterize the suspension normal stresses which are responsible for the rod-dipping or negative rod-climbing phenomenon (meaning the climbing is down instead of up the rod as seen in polymers by Beavers & Joseph 1975). This method, relying on surface deflection measurements, provides a direct determination of a linear combination of ratios of normal stress differences to shear stress which only depends on volume fraction. This permits us to circumvent divergence problems near close packing as both normal and shear stresses are supposed to present the same divergence (see e.g. Morris & Boulay 1999; Zarraga *et al.* 2000). A higher accuracy in the measurements was achieved by several enhancements of the experimental techniques, enabling the study of normal

https://doi.org/10.1017/jfm.2011.272 Published online by Cambridge University Press

stresses for a wider range of volume fractions (from 0.10 to 0.55) than in the previous studies (Zarraga *et al.* 2000; Singh & Nott 2003).

During the course of the experiments, a new time-dependent behaviour that was not reported by Zarraga *et al.* (2000) was also observed: the dip was reduced with increasing times. This time evolution was found to be related to particle migration from regions of high shear rate to regions of low shear rate and was analysed within this framework. In fact, the present rotating-rod geometry is simply the limiting case of wide-gap Couette flow for which particle migration away from the rotating inner cylinder has long been reported in the literature (Gadala-Maria & Acrivos 1980; Abott, Tetlow & Graham 1991; Tetlow 1998; Ovarlez *et al.* 2006).

Broadly speaking, two types of migration models have been proposed since the first observation of shear-induced migration. Diffusive flux models provide a kinematic description of this phenomenon in which the particle migration flux is expressed in terms of the gradients of the particle concentration and shear rate (see e.g. Leighton & Acrivos 1987). Suspension balance models relate the particle migration flux to the rheology of the suspension. They use a two-phase approach of the suspension and, from the mass and momentum balance equations of the particle phase and of the suspension as a whole, find that the particle migration flux is driven by the divergence of the normal stress of the particle phase (see Nott & Brady 1994; Morris & Boulay 1999; Lhuillier 2009; Nott, Guazzelli & Pouliquen 2011). We consider this latter type of modelling in the present study and see whether the migration phenomena are directly related to the normal stress coefficients determined experimentally. The interest of the present rotating-rod experiment lies in the combined measurements of the normal stress coefficients and migration dynamics.

The present paper is structured as follows. In § 2, the materials and methods used in the experiments are described. The linear combination of normal stress differences inferred from the rotating-rod rheometry is presented in § 3, while particle migration is analysed in § 4. These results are discussed in § 5 where conclusions are also drawn.

2. Experimental method

2.1. *Neutrally buoyant suspensions of non-Brownian spheres*

Two batches of polystyrene beads (Dynoseeds supplied by Microbeads) having a radius $a = 70 \pm 3$ and 115 ± 5 μm and density $\rho_p = 1.049 \pm 0.003$ g cm^{-3} were used in the experiments. These beads were found to be approximately spherical with a surface roughness given by the root mean square of the fluctuating roughness profile 0.2 μm, see figure 1(*d*). In order to avoid sedimentation, the Newtonian suspending fluid was chosen to be poly(ethylene glycol-ran-propylene glycol) monobutylether with density closely matched to that of the particles ($\rho_f = 1.051$ g cm^{-3} at 25 °C) and large viscosity ($\eta_f = 2.15$ Pa s). The Stokes velocity ($=(2/9)(\rho_p - \rho_f)ga^2/\eta_f$) was 0.04 and 0.1 mm h^{-1} at 25 °C for the two batches, respectively. The sedimentation effect could thus be safely neglected during the experiments that ran over a typical time scale of 1 h. The size of the particles ensured that both colloidal forces and thermal diffusion could also be neglected. The Péclet number $Pe = 6\pi\eta_f a^3\dot{\gamma}/kT \simeq 10^9\dot{\gamma}$ was always very large even at small shear rates ($\dot{\gamma} \gtrsim 10^{-2}$ s^{-1}) used in the experiments.

The suspensions were prepared by adding the polystyrene spheres into the fluid (both quantities being weighted) and by slowly stirring the mixture with a spatula. Then they were allowed to settle for more than a day at 70 °C to drive out air bubbles as the viscosity of the interstitial fluid greatly decreased at high temperatures. No sedimentation or creaming of the suspension was observed during this stage. Before

https://doi.org/10.1017/jfm.2011.272 Published online by Cambridge University Press

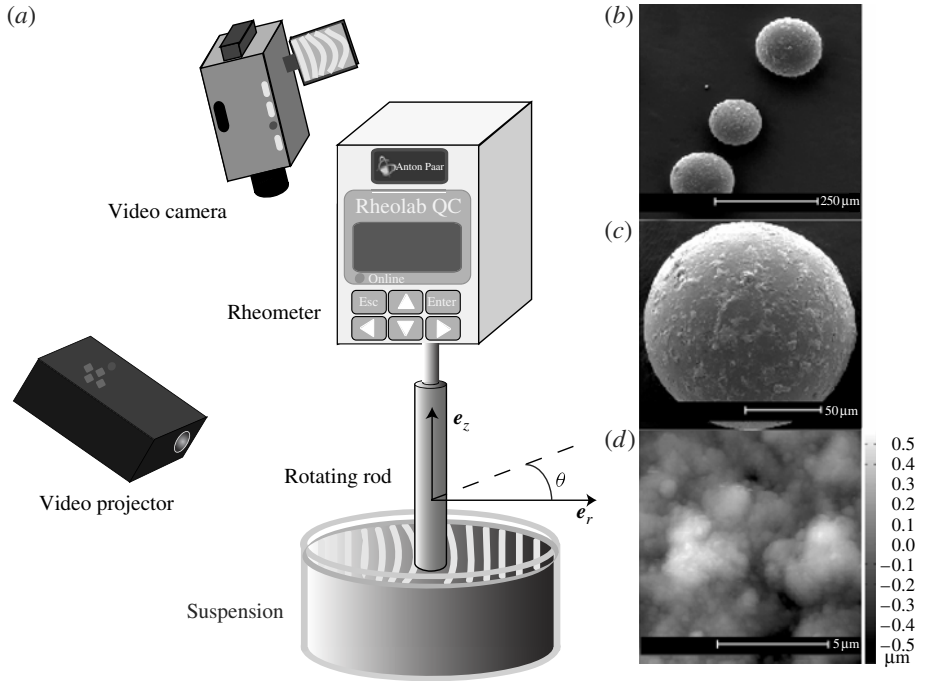


FIGURE 1. (*a*) Rotating-rod rheometer and optical profilometry setup. Micrographs of the polystyrene beads (having $a = 70 \pm 3$ µm): (*b*,*c*) scanning electron microscopy images, (*d*) atomic force microscopy topography.

each experiment, the suspension was carefully mixed to ensure that a homogeneously concentrated and reproducible initial state was reached. The surface tension γ of the suspension was measured using the Du Noüy ring method and was found to be equal to that of the suspending fluid $\gamma_f = 35$ mN m^{-1}. The particle volume fraction was varied from $\phi = 0.10$ to 0.55 in steps of 0.05.

2.2. *Rotating-rod rheometer and optical profilometry*

The experimental setup is shown in figure 1(*a*). It was adapted from the rotating-rod rheometer introduced by Beavers & Joseph (1975). It consisted of a cylindrical glass container having a radius $R_e = 55$ mm and a suspension-filled height of 65 mm. A cylindrical rod was immersed into the suspension (the typical immersed length was $L = 50$ mm, see the discussion in § 3.2). Three different rods having respective radii of $R_i = 5$, 10, and 12.5 mm were used in the experiments. In order to avoid wall-slip effects, these rods were covered with sandpaper (Barnes 1995). A rheometer (Anton Paar Rheolab QC) was used to rotate the inner rod at a fixed angular velocity ω and to measure the torque M. The shear rate was varied from $\dot{\gamma} = 50$ s^{-1} to 0.5 s^{-1} leading to particle Reynolds numbers $Re_p = \rho_p a^2 \dot{\gamma}/\eta_f$ ranging from 2×10^{-4} to 10^{-6}. Under these conditions, the Taylor number is $Ta = \rho^2 \omega^2 R_i (R_e - R_i)^3/\eta^2 \leqslant 10 \ll Ta_c \simeq 1700$, ruling out the influence Taylor vortices (Taylor 1923).

As observed by Zarraga *et al.* (2000), the negative values of normal stress differences in concentrated suspensions give rise to a negative surface deflection or rod-dipping effect, see figure 2(*c*,*d*). Accurate measurements of the free surface profile therefore require a calibrated optical setup, see figure 1. A set of parallel

https://doi.org/10.1017/jfm.2011.272 Published online by Cambridge University Press

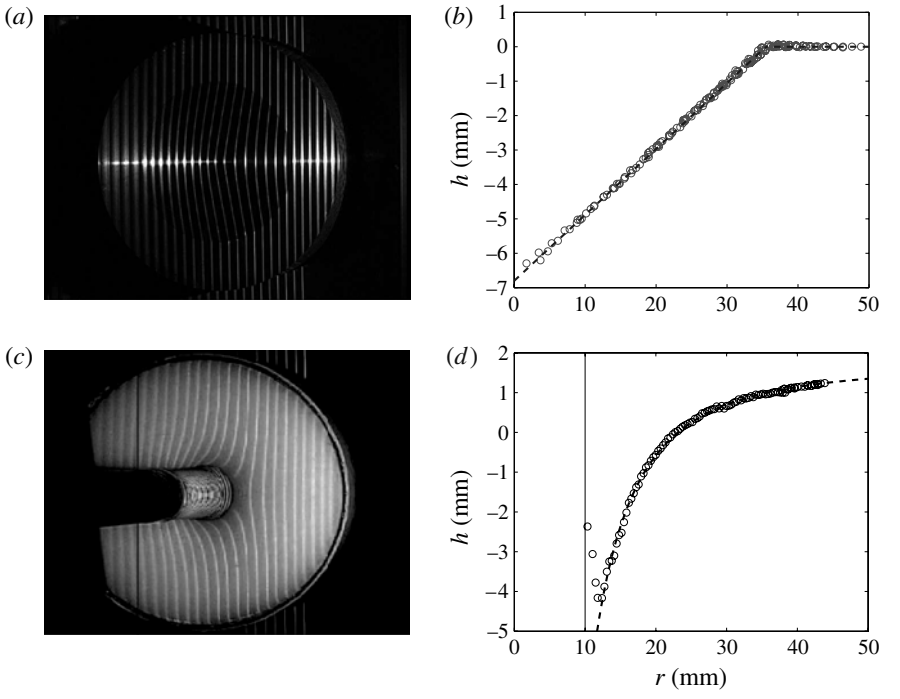


FIGURE 2. Optical profilometry calibration: (*a*) image of the inverted cone and (*b*) measured (○) and actual (dashed line) profiles. Rod dipping in a concentrated suspension with $R_i = 10$ mm and $\phi = 0.40$: (*c*) typical image of the free surface deflection and (*d*) experimental profile (○) computed from the processed image and theoretical profile $-h_0(R_i/r)^2 + h_1$ (dashed line) neglecting surface tension and inertia. The vertical solid line delineates the rod radius.

white lines were projected onto the surface of the suspension using a video projector located at a distance of 25 cm and at a fixed angle of approximately 60° from horizontal. A digital video camera positioned 70 cm above the container captured the images of the free surface. The white lines were 1 mm thick and 5 mm apart. As the local deviation of each line was proportional to the vertical displacement of the free surface, a line-tracking technique was used to compute the axisymmetric surface profile from the processed images, see figure 2. Optical calibration was performed by recording images of a ruler in the appropriate positions. To check the accuracy of the calibration, the profile of a test metallic surface (an inverted cone of radius 36 mm and depth 6.8 mm) was characterized by this profilometry technique. The experimental accuracy was found to be $\Delta h \approx 0.1$ mm (≈one particle diameter) which corresponds to $\rho g \Delta h \approx 1$ Pa, see figure 2(*a*,*b*). However, the limit of detection is approximately twice as large, as discussed in § 3. Figure 2(*c*,*d*) shows a typical image of the surface of the suspension and the corresponding computed profile.

3. Normal stresses

3.1. *Modelling rod dipping in a concentrated suspension*

Following Zarraga *et al.* (2000), we consider the suspension as an effective continuous medium and infer normal stress differences from the surface deflection of the suspension by writing the mass and momentum conservation equations for the suspension.

https://doi.org/10.1017/jfm.2011.272 Published online by Cambridge University Press

3.1.1. *Conservation and constitutive equations*

We consider a rod of radius R_i rotating at an angular velocity ω in a large bath of homogeneous suspension which is contained in a cylindrical cup of radius $R_e \gg R_i$. This geometry is similar to a Couette cylindrical system with a very large gap and a free surface.

We use a cylindrical coordinate system with origin centred at the rod centre and at a level equal to the suspension height at rest (far from the menisci). The velocity gradient direction is $\boldsymbol{e}_r$, the flow direction $\boldsymbol{e}_\theta$ and the vorticity direction $\boldsymbol{e}_z$. For small surface deflection, the velocity field is assumed to be purely azimuthal and to depend only on r

$$\boldsymbol{u} = u_\theta(r)\boldsymbol{e}_\theta. \tag{3.1}$$

The shear stress and normal stress differences of the suspension respectively read as

$$\tau = \Sigma_{r\theta}, \tag{3.2a}$$

$$N_1 = \Sigma_{\theta\theta} - \Sigma_{rr}, \tag{3.2b}$$

$$N_2 = \Sigma_{rr} - \Sigma_{zz}, \tag{3.2c}$$

where $\boldsymbol{\Sigma}$ is the total stress tensor of the suspension.

For Stokesian suspensions of non-Brownian neutrally buoyant spheres (i.e. $Pe \to \infty$ and $Re \to 0$), there is no internal time scale and dimensional analysis shows that the components of the deviatoric stress tensor are linear in shear rate $\dot{\gamma} = \sqrt{2\boldsymbol{E}:\boldsymbol{E}}$ where $\boldsymbol{E}$ is the local bulk suspension rate of strain (Stickel & Powell 2005). One can then define the suspension viscosity η_s,

$$\tau = \eta_s(\phi)\dot{\gamma}, \tag{3.3}$$

and the normal stress difference coefficients α_i ($i = 1$ or 2),

$$N_i = \alpha_i(\phi)\eta_s(\phi)\dot{\gamma} = \alpha_i(\phi)\tau. \tag{3.4}$$

Note that the α_i are defined as the ratios of the N_i with τ and thus are expected not to diverge at the maximum packing fraction ϕ_m since N_i and τ are assumed to present the same divergence as $\phi \to \phi_m$ (Morris & Boulay 1999; Zarraga *et al.* 2000).

The suspension momentum equations yield along θ, r and z, respectively,

$$\frac{\mathrm{d}}{\mathrm{d}r}(r^2\tau) = 0 \quad \text{leading to } \tau = \tau_0\left(\frac{R_i}{r}\right)^2, \tag{3.5a}$$

$$\frac{\partial}{\partial r}(\Sigma_{zz} + N_2) = \frac{N_1}{r} - \rho\frac{u_\theta^2}{r}, \tag{3.5b}$$

$$\frac{\partial \Sigma_{zz}}{\partial z} = \rho g, \tag{3.5c}$$

where $\rho = \rho_p = \rho_f$ for the neutrally buoyant suspensions considered here. Taking the jump in normal stress due to surface tension into consideration and the atmospheric pressure as a reference, the boundary condition for small deformations reads as

$$\Sigma_{zz}(r, z = h(r)) = \gamma\frac{1}{r}\frac{\mathrm{d}}{\mathrm{d}r}\left(r\frac{\mathrm{d}h}{\mathrm{d}r}\right), \tag{3.6}$$

https://doi.org/10.1017/jfm.2011.272 Published online by Cambridge University Press

where γ is the surface tension of the suspension and $h(r)$ the position of the free surface. Integration of (3.5*c*) from h to z gives

$$\Sigma_{zz}(r,z) = -\rho g[h(r)-z] + \gamma \frac{1}{r}\frac{\mathrm{d}}{\mathrm{d}r}\left(r\frac{\mathrm{d}h}{\mathrm{d}r}\right). \tag{3.7}$$

Integration of (3.5*b*) from r to R_e using the constitutive equation (3.4) finally leads to

$$\begin{aligned} -\rho g[h(r)-h(R_e)] + \gamma\left[\frac{1}{r}\frac{\mathrm{d}}{\mathrm{d}r}\left(r\frac{\mathrm{d}h}{\mathrm{d}r}\right) - \frac{1}{R_e}\frac{\mathrm{d}}{\mathrm{d}r}\left(r\frac{\mathrm{d}h}{\mathrm{d}r}\right)_{R_e}\right] \\ = \underbrace{-\left(\alpha_2+\frac{1}{2}\alpha_1\right)\tau_0}_{\rho g h_0}\left[\left(\frac{R_i}{r}\right)^2 - \left(\frac{R_i}{R_e}\right)^2\right] + \int_r^{R_e}\rho\frac{u_\theta^2}{r}\,\mathrm{d}r. \end{aligned} \tag{3.8}$$

This equation together with the mass conservation, i.e. $\int_{R_i}^{R_e} rh(r)\,\mathrm{d}r$ is equal to its value at rest, allows us to predict the free surface position $h(r)$. From (3.8), it is clear that free surface deflection is related to three physical effects: surface tension, normal stress differences and inertial effects. In the absence of surface tension and inertia, the free surface position $h(r)$ is given by

$$h(r) = -h_0\frac{R_i^2}{r^2} + h_1, \tag{3.9}$$

where

$$\rho g h_0 = -(\alpha_2 + \tfrac{1}{2}\alpha_1)\tau_0 \tag{3.10}$$

and h_1 is a constant that can be determined using the mass conservation equation (note that $h_1 = 0$ if $R_e = \infty$). Therefore, from the determination of h_0 by fitting the experimental free surface profiles, one can measure the linear combination of normal stress differences coefficients $\alpha_2 + \alpha_1/2$. Nonetheless, the influence of surface tension and inertial effects on the surface deflection have to be accounted for. These effects are examined successively in the following subsections.

3.1.2. *Influence of surface tension*

Dropping the inertial term in (3.8) gives

$$\begin{aligned} -\rho g[h(r)-h(R_e)] + \gamma\left[\frac{1}{r}\frac{\mathrm{d}}{\mathrm{d}r}\left(r\frac{\mathrm{d}h}{\mathrm{d}r}\right) - \frac{1}{R_e}\frac{\mathrm{d}}{\mathrm{d}r}\left(r\frac{\mathrm{d}h}{\mathrm{d}r}\right)_{R_e}\right] \\ = \rho g h_0\left[\left(\frac{R_i}{r}\right)^2 - \left(\frac{R_i}{R_e}\right)^2\right]. \end{aligned} \tag{3.11}$$

The two boundary conditions are given by

$$\left(\frac{\mathrm{d}h}{\mathrm{d}r}\right)_{R_i} = -\cot\theta_i \quad \text{and} \quad \left(\frac{\mathrm{d}h}{\mathrm{d}r}\right)_{R_e} = \cot\theta_e, \tag{3.12}$$

where θ_i and θ_e are the contact angles at the rod and at the external wall, respectively.

https://doi.org/10.1017/jfm.2011.272 Published online by Cambridge University Press

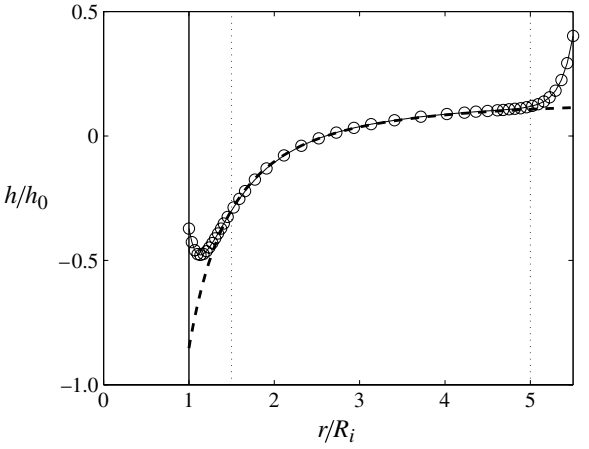


FIGURE 3. Dimensionless surface deflection h/h_0 as a function of the dimensionless radial coordinate r/R_i: $Bo = 30$ and $\theta_i = \theta_e = 45°$ (numerical solution, ○), and a zero surface tension ($-\hat{h}_1 - 1/\hat{r}^2$, dashed line). The vertical solid line delineates the rod radius while the vertical dotted lines delineate the range of validity of the zero surface tension solution.

We may recast (3.11) by using R_i as the radial length scale and $\rho g h_0$ as the pressure scale, i.e. defining the dimensionless quantities $\hat{h} = h/h_0$ and $\hat{r} = r/R_i$,

$$-(\hat{h} - \hat{h}_1) + \frac{1}{Bo}\frac{1}{\hat{r}}\frac{\mathrm{d}}{\mathrm{d}\hat{r}}\left(\hat{r}\frac{\mathrm{d}\hat{h}}{\mathrm{d}\hat{r}}\right) = \left(\frac{1}{\hat{r}}\right)^2, \tag{3.13}$$

where Bo is the Bond number $\rho g R^2/\gamma$ and $\hat{h}_1$ is the dimensionless constant

$$\hat{h}_1 = \frac{h(R_e)}{h_0} - \frac{1}{Bo}\frac{R_i}{R_e}\frac{\mathrm{d}}{\mathrm{d}\hat{r}}\left(\hat{r}\frac{\mathrm{d}\hat{h}}{\mathrm{d}\hat{r}}\right)_{R_e} - \frac{R_i^2}{R_e^2}. \tag{3.14}$$

The influence of surface tension can be studied by solving (3.13) numerically, supplemented by the mass conservation equation needed for inferring $\hat{h}_1$. Using the observed value of the contact angle of 45° on both sidewalls and the surface tension equal to that of the suspending fluid (leading to $Bo = 30$ for $R_i = 10$ mm), the numerical deflection profile is compared with the analytical solution without surface tension ($\hat{h} = \hat{h}_1 - 1/\hat{r}^2$) in figure 3. Note that this numerical solution is very similar to the experimental profile seen in figure 2(*d*). As already reported by Zarraga *et al.* (2000), surface tension effects are limited to the region close to the sidewalls. For $1.5 \lesssim \hat{r} \lesssim R_e/R_i - 0.5$, the $\hat{h}_1 - 1/\hat{r}^2$ solution coincides with the numerical solution. Thus, the zero surface tension solution can be used in the range $1.5R_i \lesssim r \lesssim R_e - 0.5R_i$ (delimited by the vertical dotted lines in figure 3). Figure 3 also shows that the negative minimum of $h(r)$ is $\approx -h_0/2$ due to the influence of the meniscus. Therefore, the limit of detection is approximately twice as large as the experimental accuracy ($\approx$0.1 mm), i.e. corresponding to $\approx$2 Pa.

3.1.3. *Influence of inertia*

In the previous analysis, we have neglected the inertial term $\int_r^{R_e} \rho(u_\theta^2/r)\,\mathrm{d}r$ in (3.8). In a finite-gap Couette cell, using the no-slip conditions on both sidewalls, the velocity

https://doi.org/10.1017/jfm.2011.272 Published online by Cambridge University Press

field is given by

$$u_\theta(r) = \omega R_i \frac{R_e^2}{R_e^2 - R_i^2}\left(\frac{R_i}{r} - \frac{R_i r}{R_e^2}\right). \tag{3.15}$$

From (3.15) the integration of the inertial term gives

$$-\int_r^{R_e} \rho\,(u_\theta^2/r)\,\mathrm{d}r = -\frac{\rho\omega^2 R_i^2}{2}\frac{R_e^2}{R_e^2 - R_i^2}\left[\frac{R_i^2}{r^2} + \frac{R_i^2}{R_e^2}\left(4\log\left(\frac{r}{R_e}\right) - \frac{r^2}{R_e^2}\right)\right]$$
$$\equiv \rho g h_{in}(r). \tag{3.16}$$

This term scales as $\rho\omega^2 R_i^2$ and has to be compared in (3.8) with the normal stress difference which scales as $\alpha_i \eta_s \omega$ (see (3.4)). Inertia only plays a role at high rotation speed and is negligible most of the time (below the sensitivity of the optical profilometry technique). Nonetheless, the inertial contribution h_{in} has to be subtracted from the measured deflection to obtain the sole contribution of the normal stress differences. One can then conveniently define a modified profile $h^\star = h - h_{in}$. As a result, $h^\star$ verifies (3.9) in the range $1.5R_i \lesssim r \lesssim R_e - 0.5R_i$ where surface tension can be neglected.

3.2. *Experiments*

3.2.1. *Experimental procedure*

From the theoretical considerations developed in the preceding section, the following experimental procedure is used to infer the normal stress coefficient $\alpha_1/2 + \alpha_2$:

(*a*) the surface deflection $h(r)$ is measured in the region far from the two sidewalls, where surface tension effects are negligible ($1.5R_i \lesssim r \lesssim R_e - 0.5R_i$);

(*b*) the inertial contribution is subtracted to the observed deflection by defining a modified deflection $h^\star(r) = h(r) - h_{in}(r)$ using (3.16);

(*c*) the deflection h_0 due to the sole effect of normal stresses is computed by fitting $h^\star(r)$ by a $h_1 - h_0(R_i/r)^2$ function, see figure 2(*d*);

(*d*) the normal-stress coefficient $\alpha_2 + (1/2)\alpha_1$ is given by the slope of the linear variation of $\rho g h_0$ with τ_0 using (3.10); the shear stress at the rod τ_0 is calculated from the measured torque M as $\tau_0 = M/2\pi L R_i^2$, where L is the immersed length of the rod and R_i its radius.

3.2.2. *Experimental results*

Here, the analysis of the experimental results is limited to time-independent data obtained at short times (typically 1 min). In this case, migration processes can be neglected (see § 4 for the analysis of long time migration effects) and, since the suspension is homogeneous, the model presented in § 3.1 applies.

Prior to determining $\alpha_2 + \alpha_1/2$, the influence of the radius R_i and immersed length L of the rod was examined. Figure 4(*a*) displays $\rho g h_0$ versus $\tau_0 = M/2\pi L R_i^2$ for three different radii but for the same suspension. The data coming from the different rod measurements collapse on the same straight line as expected from (3.10). Figure 4(*b*) presents $\rho g h_0$ versus L for the same suspension. It clearly shows that, for $L \geqslant 40$ mm, the measurements are independent of the immersed length L. Moreover, the measured torque M is found to be linear in L showing that wall effects are negligible, see the inset of figure 4(*b*). In the measurements presented in the following, the immersed length was chosen to be $L = 50$ mm.

Figure 5 shows $\rho g h_0$ versus τ_0 for four different volume fractions $\phi = 0.2$, 0.3, 0.4 and 0.5. Clearly, the normal stress $\rho g h_0$ is seen to be linear in shear stress τ_0

https://doi.org/10.1017/jfm.2011.272 Published online by Cambridge University Press

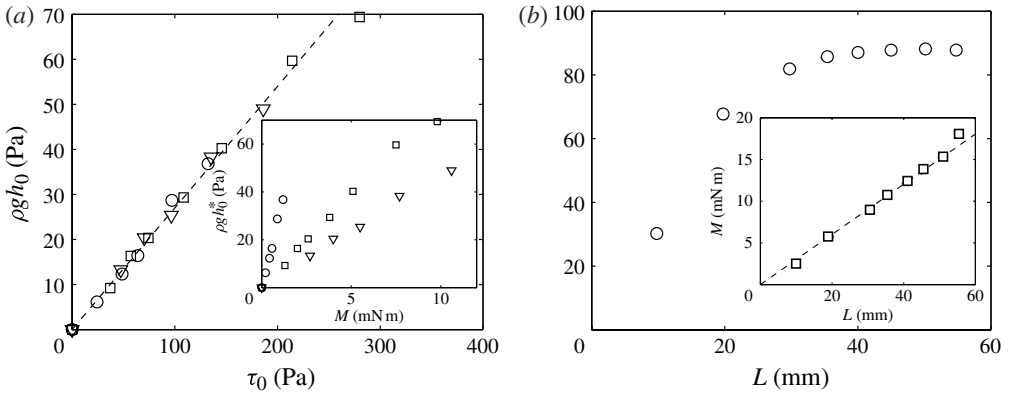


FIGURE 4. (*a*) Normal stress $\rho g h_0$ versus shear stress τ_0 for three different rod radii: $R_i = 5$ mm (○), 10 mm (□) and 12.5 mm (▽). Inset: $\rho g h_0$ versus torque M for the same three rods. (*b*) Normal stress $\rho g h_0$ versus immersed length L. Inset: torque M versus L. Data are obtained for $\phi = 0.4$ and $a = 70 \pm 3$ μm.

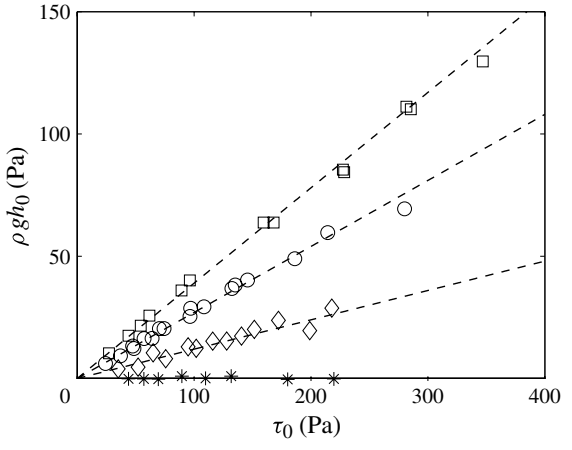


FIGURE 5. (*a*) Normal stress $\rho g h_0$ versus shear stress τ_0 for different solid volume fractions: $\phi = 0.2$ (∗), $\phi = 0.3$ (◇), $\phi = 0.4$ (○) and $\phi = 0.5$ (□). Dashed lines: linear regressions.

which confirms the anticipated viscous scaling, see (3.4). It has been fitted to a linear function of τ_0 using the method of weighted least squares (see e.g. Taylor 1982). This provides the slope $-(\alpha_2 + (1/2)\alpha_1)$ (see (3.10)) with a fractional uncertainty of ≈ 0.1. For $\phi < 0.25$, no surface deflection and thus no normal stress difference can be detected within the detection limit of ≈ 2 Pa. The variation of $-(\alpha_2 + (1/2)\alpha_1)$ with ϕ is shown in figure 6.

For $\phi < 0.25$, as mentioned above, the deflection (if any) is below the detection limit meaning that $-(\alpha_2 + (1/2)\alpha_1) \lesssim 0.02$. In this concentration range, only numerical and analytical predictions are available as shown in the inset of figure 6. We have thus reported the predictions of the numerical simulations of Sierou & Brady (2002) and the analytical predictions of Wilson (2005) using her calculations of the normal stress ϕ^2-coefficient (her figure 3) with a roughness height of 0.2 μm as experimentally measured, see figure 1 and § 2.1. The expected magnitude of the normal stress

https://doi.org/10.1017/jfm.2011.272 Published online by Cambridge University Press

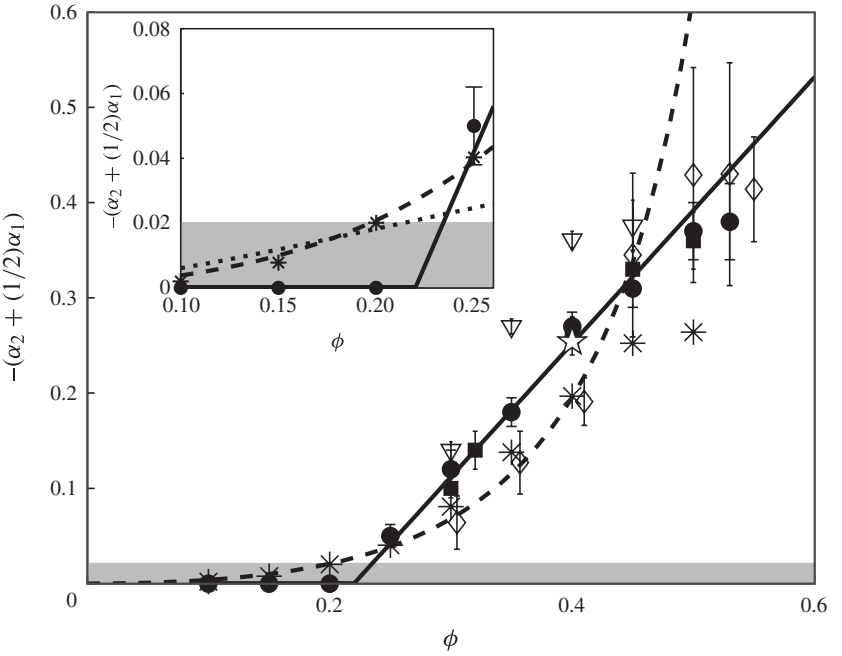


FIGURE 6. Normal stress difference coefficient $-(\alpha_2 + (1/2)\alpha_1)$ versus volume fraction ϕ. Present experiments: $a = 70 \pm 3$ μm (•) and $a = 115 \pm 5$ μm (■). Previous experiments: Zarraga *et al.* (2000) (◇), Singh & Nott (2003) (▽). Stokesian dynamics simulations: Sierou & Brady (2002) without sliding friction (∗) and with a friction coefficient of 0.5 (white star). Linear fit: $1.4(\phi - \phi_c)$ (solid line). Correlation: Morris & Boulay (1999) (dashed line). Inset: enlarged view of low ϕ and comparisons with the simulations of Sierou & Brady (2002) without friction (∗), the analytical calculations of Wilson (2005) with a roughness height of 0.2 μm (dotted line), the correlation of Morris & Boulay (1999) (dashed line) and the linear fit $1.4(\phi - \phi_c)$ (solid line). The limit of detection is indicated in grey.

coefficients are very small and therefore the predicted $-(\alpha_2 + (1/2)\alpha_1)$ are below the detection limit of the present apparatus.

For $\phi \gtrsim 0.25$, there is a clear behavioural change. The normal stress coefficient combination $-(\alpha_2 + (1/2)\alpha_1)$ seems to be linear and can be fitted by $1.4(\phi - \phi_c)$ with $\phi_c = 0.22 \pm 0.01$ (solid line). The data coming from the two different batches of particles collapse on the same straight line, thus showing no dependence on particle size (black filled symbols). The overall increase is similar to that found in previous experiments (Zarraga *et al.* 2000; Singh & Nott 2003) (open symbols) and Stokesian dynamics simulations (Sierou & Brady 2002) (∗). As raised in the introduction, there can be a factor of two difference between the data of Zarraga *et al.* (2000) for glass spheres (◇) and Singh & Nott (2003) for polymethyl methacrylate (PMMA) spheres (▽), with those of Zarraga *et al.* (2000) being smaller than those of Singh & Nott (2003). The present data for polystyrene spheres (filled symbols) lie in between below $\phi = 0.45$, but become smaller (or of the same order) than the data of Zarraga *et al.* (2000) above. Whether the discrepancy between the different experimental data obtained for different types of particles can be attributed to their surface properties (roughness and friction) is still an open issue. The role of friction can be evidenced when comparing with the predictions of the Stokesian dynamics simulations (Sierou & Brady 2002). Without sliding friction between the particles (∗), the numerical data are

https://doi.org/10.1017/jfm.2011.272 Published online by Cambridge University Press

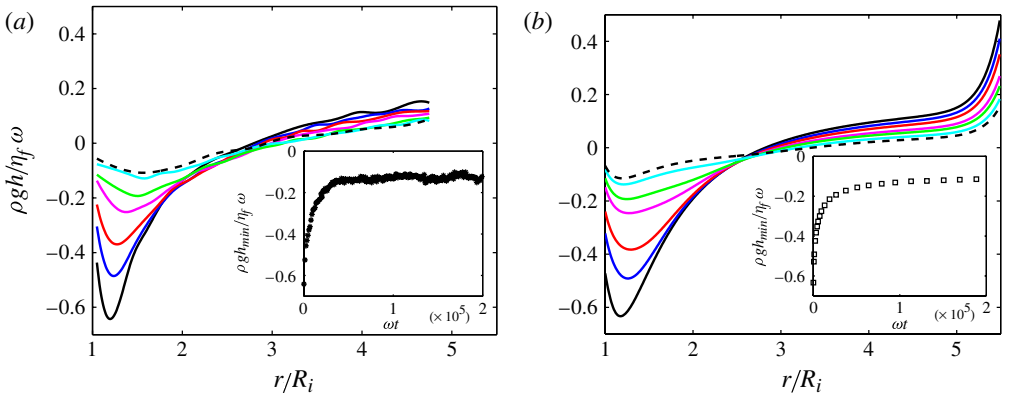


FIGURE 7. (Colour online available at journals.cambridge.org/flm) Evolution of the dimensionless free surface deflection profiles $\rho gh/\eta_f\omega$ with dimensionless time (or strain) ωt for a suspension of spheres of $a = 70 \pm 3$ μm initially at $\phi = 0.4$ for $\omega t = 0$ (black line), $\omega t = 10^3$ (blue line), $\omega t = 3 \times 10^3$ (red line), $\omega t = 10^4$ (magenta line), $\omega t = 3 \times 10^4$ (green line), $\omega t = 10^5$ (cyan line) and $\omega t = 2 \times 10^5$ (dashed black line), coloured lines from blue to cyan are represented by decreasing shades of grey in the print version. Insets: profile minimum versus dimensionless time (or strain). (*a*) Experimental data. (*b*) Numerical predictions using (4.12*b*).

always smaller than the present measurements (filled symbols) while better agreement is obtained when the effect of friction is included in the simulations (white star) for $\phi = 0.40$ with a friction coefficient of 0.5. The correlation proposed by Morris & Boulay (1999) is also shown on the same figure (this correlation will be presented with further details in § 4, see (4.13)). While this correlation shows reasonable agreement with the experiments of Zarraga *et al.* (2000) and the simulations of Sierou & Brady (2002) for $\phi \lesssim 0.45$, a simple linear correlation seems to better match the present experimental results.

4. Particle migration

4.1. *Observations*

The present experiment exhibits a time-dependent behaviour that has not been reported by Zarraga *et al.* (2000). The free surface deflection h presents a time evolution in which the dip is strongly reduced with increasing time, see figure 7(*a*). Note that the data reported for initial time ($t = 0$ min) are those used in § 3 to infer the normal stress differences of the suspension. The surface deflection decreases and the minimum moves toward larger radial distances with increasing time.

Measurements of the volume fraction were performed by taking samples using a plastic pipette (the tip was enlarged to 1 cm by cutting the end) at different radial distances. Each sample was weighted (approximatively 2.5 g) then immersed into a large quantity of water, filtered and dried. Volume fractions were obtained as the ratio of the mass of the particles to the mass of the sample. Note that this basic method proved to be fairly accurate as the spatially averaged volume fraction gives the initial volume fraction with less than 5 % discrepancy. Examination of the experimental data (□) in figure 8 shows that after the largest strain achieved in the experiments, $\omega t = 2 \times 10^5$, the suspension is no longer uniform across the container but presents an increase of volume fraction ϕ with radial distance. This is consistent with the previous

https://doi.org/10.1017/jfm.2011.272 Published online by Cambridge University Press

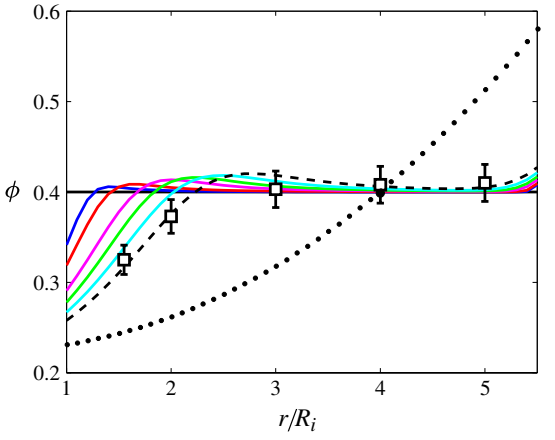


FIGURE 8. (Colour online) Evolution of the volume fraction profiles $\phi(r/R_i)$ with dimensionless time (or strain) ωt for the same suspension as figure 7 initially at $\phi = 0.4$ (horizontal solid line). Numerical predictions using (4.12*b*) for the same values of ωt as in figure 7 (black, blue, red, magenta, green, cyan and dashed black lines) and at steady state, i.e. $\omega t = \infty$ (dotted line). Experimental data at $\omega t = 2 \times 10^5$ (□) (to be compared with the dashed black line).

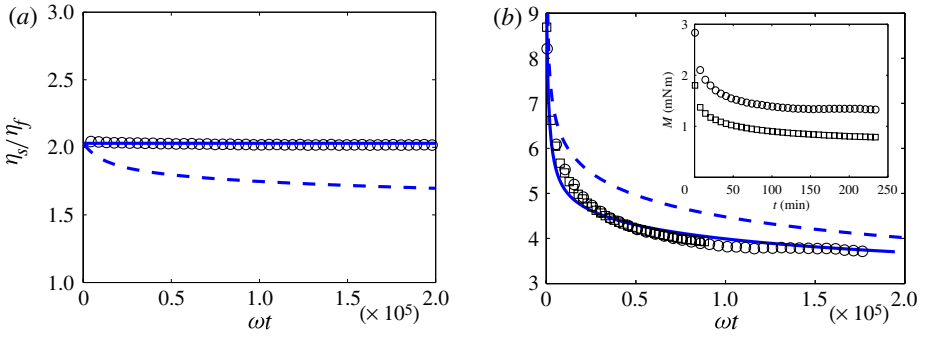


FIGURE 9. (Colour online) Apparent relative viscosity η_s/η_f versus dimensionless time (or strain) ωt for a suspension of spheres of $a = 70 \pm 3$ μm. Experiments: $\omega = 60$ r.p.m. (□) and $\omega = 120$ r.p.m. (○). Numerical predictions (blue online) using (4.12*b*) (thick solid line) and (4.13) (thick dashed line). (*a*) Initial volume fraction $\phi = 0.2$. (*b*) Initial volume fraction $\phi = 0.4$. Inset: torque M versus time.

observation of time-dependent behaviour and is strong evidence of particle migration from regions of high shear rate to regions of low shear rate.

The torque M is also found to evolve with time and more precisely to decrease on the same time scale as the filling of the dip shown in figure 7(*a*). Evidence of this is shown in the inset of figure 9(*b*) where one can see that the measured torque dropped by approximately 50 % at $\phi = 0.4$. In this figure, the torque evolution is shown for two different rotation speeds. Collapse of the data is obtained in the main figure 9(*b*) by plotting the apparent relative viscosity $\eta_s/\eta_f = M/4\pi LR^2\omega\eta_f$ versus dimensionless time (or strain) ωt. Clearly, the migration process is controlled by strain. Also, no evolution of η_s/η_f and therefore no migration is observed for $\phi \lesssim 0.2$ as can be seen in figure 9(*a*) for $\phi = 0.2$.

https://doi.org/10.1017/jfm.2011.272 Published online by Cambridge University Press

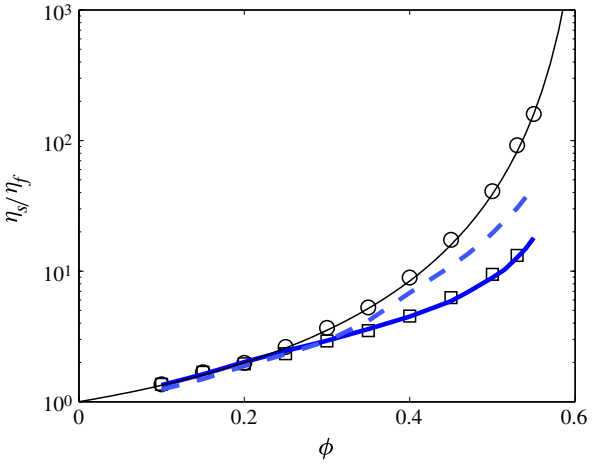


FIGURE 10. (Colour online) Apparent relative viscosity η_s/η_f versus initial solid volume fraction. Experiments: initial (○) and at $\omega t = 2 \times 10^5$ (□). Empirical correlation: Zarraga *et al.* (2000) (thin black solid line). Numerical predictions (blue online) at $\omega t = 2 \times 10^5$ using (4.12*b*) (thick solid line) and (4.13) (thick dashed line).

An alternative indication of the evolution of the relative viscosity is given in figure 10. The initial relative viscosity η_s/η_f is found to be well fitted by the empirical function proposed by Zarraga *et al.* (2000) (solid line in figure 10)

$$\eta_s(\phi)/\eta_f = \exp(-2.34\phi)\left(1 - \frac{\phi}{\phi_m}\right)^{-3}, \tag{4.1}$$

with $\phi_m = 0.62$. We have also plotted in this figure the apparent relative viscosity deduced from torque measurements for the largest values of the strain obtained experimentally ($\omega t = 2 \times 10^5$) versus the initial volume fraction. Again, for $\phi \lesssim 0.2$, there is no measurable difference between the initial and long-time values of η_s/η_f and thus no detectable migration.

4.2. *Modelling particle migration*

4.2.1. *The suspension balance model*

The suspension balance model is based on a two-phase formulation written at low Reynolds number (see e.g. Nott & Brady 1994; Morris & Boulay 1999). It is usually expressed for the suspension (i.e. the entire mixture) and the solid phase.

The balance equations for the entire suspension are, as previously described in § 3.1,

$$\boldsymbol{\nabla} \cdot \boldsymbol{u} = 0, \tag{4.2a}$$

$$\boldsymbol{\nabla} \cdot \boldsymbol{\Sigma} + \rho \boldsymbol{g} = 0, \tag{4.2b}$$

where $\boldsymbol{\Sigma}$ is the total stress tensor of the suspension and $\boldsymbol{u} = \phi \boldsymbol{u}^p + (1-\phi)\boldsymbol{u}^f$ is the volume average velocity of the suspension ($\boldsymbol{u}^p$ and $\boldsymbol{u}^f$ are the local mean particle and fluid velocities, respectively).

The balance equations for the particle phase in a neutrally buoyant system are

$$\frac{\partial \phi}{\partial t} + \boldsymbol{\nabla} \cdot (\phi \boldsymbol{u}^p) = 0, \tag{4.3a}$$

$$\boldsymbol{\nabla} \cdot \boldsymbol{\Sigma}^p + \boldsymbol{F} = 0, \tag{4.3b}$$

where $\boldsymbol{\Sigma}^p$ is the particle-phase stress and $\boldsymbol{F}$ is the inter-phase drag force.

https://doi.org/10.1017/jfm.2011.272 Published online by Cambridge University Press

The drag force, which depends on particle concentration and is proportional to the relative velocity, is usually modelled as

$$\boldsymbol{F} = -\frac{9\eta_f}{2a^2}\frac{\phi}{f(\phi)}(\boldsymbol{u}^p - \boldsymbol{u}), \tag{4.4}$$

where one can use the empirical law $f(\phi) = (1-\phi)^n$ (with $n \simeq 5$ at low Reynolds numbers) proposed by Richardson & Zaki (1954).

Using the incompressibility of the suspension (4.2*a*), the particle mass conservation equation (4.3*a*) can be written as

$$\begin{aligned}\frac{\partial \phi}{\partial t} + \boldsymbol{u}\cdot\boldsymbol{\nabla}\phi &= -\boldsymbol{\nabla}\cdot[\phi(\boldsymbol{u}^p - \boldsymbol{u})],\\ &= -\frac{2a^2}{9\eta_f}\boldsymbol{\nabla}\cdot[f(\phi)\boldsymbol{\nabla}\cdot\boldsymbol{\Sigma}^p],\end{aligned} \tag{4.5}$$

using (4.3*b*) and (4.4). This equation relates the cross-stream migration of particles to the normal stresses of the particle phase through a migration flux

$$\boldsymbol{j}_\perp = \phi(\boldsymbol{u}^p - \boldsymbol{u}) = (2a^2/9\eta_f)f(\phi)\boldsymbol{\nabla}\cdot\boldsymbol{\Sigma}^p. \tag{4.6}$$

As the particle flux is proportional to the square of the particle radius, migration dynamics is dramatically faster in suspensions of larger particles. Note that non-diagonal components of the particle phase stress tensor will not generate any cross-stream migration flux. In the following, the non-diagonal terms of $\boldsymbol{\Sigma}^p$ have been dropped and $\boldsymbol{\Sigma}^p$ now refers to the normal stress tensor of the particle phase.

4.2.2. *Constitutive equations for the particle-phase stress*

Since the present experiments do not enable us to provide a direct measurement of the particle-phase stress, it is necessary to assume a phenomenological form, inject it into the balance equations and compare these predictions with the experimental results.

We chose to use a form having a viscous scaling and a similar ϕ dependence in all of the directions

$$\boldsymbol{\Sigma}^p = -\eta_f\dot{\gamma}\hat{\eta}_n(\phi)\begin{pmatrix}1 & 0 & 0\\ 0 & \lambda_2 & 0\\ 0 & 0 & \lambda_3\end{pmatrix}, \tag{4.7}$$

where $\hat{\eta}_n(\phi)$ is a dimensionless 'normal viscosity' defined as $\hat{\eta}_n(\phi) = -\Sigma^p_{11}/\eta_f\dot{\gamma}$ and λ_2 and λ_3 are two scalar parameters which are independent of ϕ (Morris & Boulay 1999). Note that this expression for $\boldsymbol{\Sigma}^p$ is consistent with the experimental observation that the migration flux does not depend on the fluid viscosity as

$$\boldsymbol{j}_\perp = -\frac{2a^2}{9}f(\phi)\boldsymbol{\nabla}\cdot\left[\dot{\gamma}\hat{\eta}_n(\phi)\begin{pmatrix}1 & 0 & 0\\ 0 & \lambda_2 & 0\\ 0 & 0 & \lambda_3\end{pmatrix}\right]. \tag{4.8}$$

Following again Morris & Boulay (1999), we assume that the normal stress differences of the particle phase are identical to those of the whole suspension (this assumption is discussed in § 5). In other words, the stress of the fluid phase $\boldsymbol{\Sigma}^f$ is assumed to be Newtonian so that $\Sigma^f_{11} = \Sigma^f_{22} = \Sigma^f_{33}$. The particle-phase pressure Π and the normal stress differences that arise in curvilinear flows are defined as

$$\Pi = -\tfrac{1}{3}\mathrm{Tr}(\boldsymbol{\Sigma}^p), \tag{4.9a}$$

https://doi.org/10.1017/jfm.2011.272 Published online by Cambridge University Press

$$N_1 = \Sigma_{11} - \Sigma_{22} = \Sigma^p_{11} - \Sigma^p_{22}, \tag{4.9b}$$

$$N_2 = \Sigma_{22} - \Sigma_{33} = \Sigma^p_{22} - \Sigma^p_{33}. \tag{4.9c}$$

Therefore,

$$\frac{\Pi}{\eta_f \dot{\gamma}} = \frac{1 + \lambda_2 + \lambda_3}{3} \hat{\eta}_n(\phi), \tag{4.10a}$$

$$\frac{N_1}{\eta_f \dot{\gamma}} = (\lambda_2 - 1)\hat{\eta}_n(\phi), \tag{4.10b}$$

$$\frac{N_2}{\eta_f \dot{\gamma}} = (\lambda_3 - \lambda_2)\hat{\eta}_n(\phi). \tag{4.10c}$$

Consequently, in this model, the normal stress viscosity $\hat{\eta}_n(\phi)$ and the anisotropy coefficients λ_i of the particle-phase stress tensor can be inferred from rheological measurements of normal stress differences of the whole suspension. We can then relate the normal stress coefficients determined in § 3.2 to these parameters

$$\alpha_2 + \frac{\alpha_1}{2} = \frac{N_2 + \dfrac{N_1}{2}}{\tau} = -\frac{1 + \lambda_2 - 2\lambda_3}{2} \frac{\hat{\eta}_n}{\hat{\eta}_s}, \tag{4.11}$$

where $\hat{\eta}_s = \eta_s/\eta_f$ is the dimensionless suspension viscosity. A complete determination of $\eta_n(\phi)$ and of the λ_i requires additional independent normal stress measurements. Reliable values of λ_i can be found in the literature as they are consistent with the experimental facts that (i) both normal stress differences are negatives, (ii) $|N_2| > |N_1|$ and (iii) no particle migration is observed in a parallel-plate geometry. A compatible set of parameters is $\lambda_2 = 0.85$ and $\lambda_3 = 0.5$ (Morris & Boulay 1999; Zarraga *et al.* 2000). Using these values for the λ_i and the normal stress coefficient deduced from the present experiments reported in § 3.2 (solid line in figure 6), the ratio of normal to shear viscosities is given by

$$\frac{\hat{\eta}_n}{\hat{\eta}_s} = 0 \quad \text{for } \phi < \phi_c \tag{4.12a}$$

$$\frac{\hat{\eta}_n}{\hat{\eta}_s} = 3.3(\phi - \phi_c) \quad \text{for } \phi \geqslant \phi_c \tag{4.12b}$$

with $\phi_c = 0.22$. For closing the model, we choose the empirical correlation (4.1) for the relative viscosity proposed by Zarraga *et al.* (2000) which happens to fit very well with the experimental data as shown in § 4.1 (solid line in figure 10). Note that the choice of another viscosity function among those commonly used to model the dense regime rheology would have only a slight effect on the predictions of the model.

In the following, we also provide predictions using the expression for $\hat{\eta}_n/\hat{\eta}_s$ proposed by Morris & Boulay (1999) (dashed line in figure 6)

$$\frac{\hat{\eta}_n}{\hat{\eta}_s} = \frac{0.75\left(\dfrac{\phi}{\phi_m}\right)^2 \left(1 - \dfrac{\phi}{\phi_m}\right)^{-2}}{1 + 2.5\phi_m \left(1 - \dfrac{\phi}{\phi_m}\right)^{-1} + 0.1\dfrac{\phi}{\phi_m}^2 \left(1 - \dfrac{\phi}{\phi_m}\right)^{-2}}, \tag{4.13}$$

with $\phi_m = 0.62$.

https://doi.org/10.1017/jfm.2011.272 Published online by Cambridge University Press

4.2.3. *Implementation of the model*

From (4.5) and (4.7), a partial differential equation for the volume fraction ϕ is obtained

$$\frac{\partial \phi}{\partial t} + \boldsymbol{u} \cdot \boldsymbol{\nabla} \phi = \frac{2a^2}{9} \boldsymbol{\nabla} \cdot \left\{ (1-\phi)^5 \boldsymbol{\nabla} \cdot \left[\dot{\gamma}\, \hat{\eta}_n(\phi) \begin{pmatrix} 1 & 0 & 0 \\ 0 & \lambda_2 & 0 \\ 0 & 0 & \lambda_3 \end{pmatrix} \right] \right\}. \tag{4.14}$$

The order of magnitude of the term of the right-hand side of this equation (i.e. the divergence of the migration flux) is given by $\dot{\gamma} a^2 / R_i^2 \ll \dot{\gamma}$. This indicates that the cross-stream migration dynamics is much slower than the mean shear flow dynamics. Therefore, in the rotating-rod calculation presented in § 3.1, the volume average velocity $\boldsymbol{u}$ can still be assumed to be purely azimuthal and to depend only on r. In the following calculations, the immersed length of the rod is assumed to be large enough to neglect any z-dependence. Consequently, ϕ is a function of the radial coordinate r and time t and the term $\boldsymbol{u} \cdot \boldsymbol{\nabla} \phi$ can be dropped. Equation (4.14) becomes

$$\frac{\partial \phi}{\partial t} = \frac{2a^2}{9} \frac{(1/r)\partial}{\partial r} \left[r(1-\phi)^5 \left(\lambda_2 \frac{\partial \hat{\eta}_n \dot{\gamma}}{\partial r} + (\lambda_2 - 1) \frac{\hat{\eta}_n \dot{\gamma}}{r} \right) \right]. \tag{4.15}$$

The local shear rate $\dot{\gamma}(r)$ needs to be determined at each time step. As discussed above, the flow is assumed to be stationary with respect to the migration dynamics: for each transient volume fraction profile, one has to solve the momentum equation (3.5*a*) for the mixture but with a local viscosity no longer constant across the gap:

$$\frac{\partial}{\partial r}(r^2 \tau) = 0 \quad \text{leading to} \quad \frac{\partial}{\partial r}(r^2 \eta_s \dot{\gamma}) = 0. \tag{4.16}$$

As the rotational velocity of the rod is a fixed external control parameter, this latter equation can be written in terms of velocity u_θ since $\dot{\gamma} = \partial u_\theta / \partial r - u_\theta / r$,

$$\frac{\partial^2 u_\theta}{\partial r^2} + \frac{1}{\eta_s} \frac{\partial \eta_s r}{\partial r} \left[\frac{1}{r} \frac{\partial u_\theta}{\partial r} - \frac{u_\theta}{r^2} \right] = 0. \tag{4.17}$$

In order to solve the system of (4.15) and (4.17) numerically, a finite difference method was developed: (i) with a forward difference for the time derivative and a second-order central difference for the space derivative (4.15); and (ii) with a forward difference for the first-order and central difference for the second-order space derivative (4.17). The boundary conditions are given by

$$\boldsymbol{j}_\perp = 0 \quad \text{and} \quad u_\theta = \omega R_i \quad \text{for } r = R_i, \tag{4.18}$$

$$\boldsymbol{j}_\perp = 0 \quad \text{and} \quad u_\theta = 0 \quad \text{for } r = R_e. \tag{4.19}$$

The free surface deflection is obtained by solving (3.8) numerically.

We can also compute the steady-state concentration at the end of the migration process by imposing a zero flux. Equation (4.15) becomes

$$\lambda_2 \frac{\partial \hat{\eta}_n \dot{\gamma}}{\partial r} + (\lambda_2 - 1) \frac{\hat{\eta}_n \dot{\gamma}}{r} = 0, \tag{4.20}$$

which leads to

$$\frac{\hat{\eta}_n}{\hat{\eta}_s}(\phi) \propto r^{(1+\lambda_2)/\lambda_2}. \tag{4.21}$$

https://doi.org/10.1017/jfm.2011.272 Published online by Cambridge University Press

The concentration profile $\phi(r)$ is obtained by injecting the chosen constitutive relation in the above equation and requiring $\phi(r)$ to average to the imposed initial concentration.

The numerical predictions of the model using the two different constitutive relations for $\eta_n(\phi)$ given by (4.12*b*) and (4.13) are compared with the experimental observations in the following section. Note that both predictions use the same values for λ_2 and λ_3 as those proposed by Morris & Boulay (1999) and Zarraga *et al.* (2000). Note however that the choice of slightly different anisotropy coefficients, e.g. $0.8 \lesssim \lambda_2 \lesssim 1$, does not have a significant effect on these predictions.

4.3. *Comparison of experimental data with predictions*

The evolution of the free surface deflexion with time in a suspension of spheres ($a = 70 \pm 3$ μm) initially at $\phi = 0.4$ is shown in figure 7. A quantitative agreement between experimental (figure 7*a*) and numerical results (figure 7*b*) is obtained: the shape of the surface deformation during the migration process as well as the depth amplitude h_{min} are well predicted by the model. The comparison is only shown for the constitutive relation (4.12*b*) but similar qualitative behaviour is obtained when using relation (4.13).

The decay of the apparent relative viscosity (deduced from torque measurements) with strain is also compared with the numerical predictions in figure 9 for $\phi = 0.2$ and 0.4. Good agreement between the experiments and the numerical predictions (thick solid line, blue online) using normal stresses measured for the suspension in § 3, i.e. using (4.12*b*), is again observed for both volume fractions. Using the correlation proposed by Morris & Boulay (1999) for the normal stress differences, i.e. using (4.13), yields poorer agreement (thick dashed line, blue online). It is important to stress that no variation of η_s/η_f and therefore no migration is observed for $\phi \lesssim 0.2$, see figure 9(*a*), in contrast with the decay predicted by the correlation of Morris & Boulay (1999). However, at these low concentrations, the migration phenomenon may be influenced by inertial secondary currents driven by end effects. The circulation time of this secondary vortex over the radial gap (a flow upward from the bottom of the container in the vicinity of the rotating rod and radially outward along its length) has been evaluated by visualizing the evolution of a bit of dye in the cell filled with the pure fluid at the same angular velocity ω as used in the low-ϕ experiments. It corresponds to a dimensionless time of $\omega t \approx 0.2 \times 10^5$ which is of the same order of magnitude as the migration time scale predicted by Morris & Boulay (1999), see figure 9(*a*). Whether this effect is able to mix the suspension and thus hinder migration is an open issue as a detailed analysis would be required to examine the coupling between migration and secondary flows.

Figure 8 shows the predictions of the model for the particle concentration along the r-axis for different values of the applied strain ωt. In the same figure, the predicted steady-state concentration profile (dotted line) is also plotted. It is worth noting that, even for the largest experimental strain ($\omega t = 2 \times 10^5$), the migration process is far from being completely achieved. In the experiments, larger strain values ($\omega t \gg 2 \times 10^5$) were not investigated as it would have required either longer experiments where sedimentation and temperature fluctuations can no longer be neglected, or higher rotational speeds leading to possible inertial effects at the particle scale which are out of the focus of this study. Nonetheless, the experimental (□) and numerical (dashed line) profiles are in good agreement at $\omega t = 2 \times 10^5$.

Comparison between numerical simulations and experimental data for the apparent relative viscosity versus ϕ at $\omega t \approx 2 \times 10^5$ (largest strain obtained in the experiments)

https://doi.org/10.1017/jfm.2011.272 Published online by Cambridge University Press

is shown in figure 10. Excellent agreement is obtained when using the normal stresses measured for the suspension in § 3, i.e. using (4.12*b*). Again, poorer agreement is obtained when using the relation proposed by Morris & Boulay (1999), i.e. using (4.13).

5. Concluding remarks

In this paper, we have reported measurements of a linear combination of normal stress differences in a suspension of neutrally buoyant spheres. The suspension is submitted to a flow induced by a rotating rod which is similar to a Couette cylindrical system with a very large gap and a free surface. A negative surface deflection, i.e. negative rod climbing or rod dipping, is observed and measured using an accurate optical profilometry technique. The normal stress differences are inferred from these measurements using a continuum modelling of the suspension. These differences are seen to be linear in shear stress. This demonstrates that a viscous scaling is appropriate. For dilute suspensions, the ratio of normal stress differences to the shear stress is smaller than 2 %, which is the detection limit of the apparatus. Above a volume fraction of approximatively 0.22, it is seen to increase drastically with increasing concentration.

These data suggest a behavioural change around 0.22 which was not reported in previous experiments (Zarraga *et al.* 2000; Singh & Nott 2003) where measurements were not undertaken below a concentration of 0.3. This change is even more evidenced in following measurements of a second normal stress difference using the examination of the deflection of the suspension free surface (with a lower detection limit) in a tilted trough flow (Couturier *et al.* 2011). It seems only to be fully captured by Stokesian dynamics simulations (Sierou & Brady 2002) when frictional contacts are included. The origin of normal stress differences is far from being understood completely. However, they may arise from hydrodynamic interactions or direct contact between particles in the case of non-Brownian (non-colloidal) particles (see e.g. Morris 2009). The observed strong increase around 0.2 seems to suggest that the role of contacts may be crucial since hydrodynamic interactions are supposed to act at all concentrations while contacts may only occur above a critical concentration (it is interesting to note that the percolation threshold for a transient infinite cluster corresponds precisely to a concentration of 0.2, see De Gennes 1979). The effect of contacts is twofold as normal stresses can originate from either the flow-induced structure due to the non-hydrodynamic effects of the contacts (see e.g. Wilson 2005) or the direct contact forces. At that point of the discussion, one cannot tell which of the effects is dominant, but the following discussion will bring some further conclusions.

The above results are obtained just after submitting the suspension to the rotating-rod flow. When the experiments are run longer, the initial dip reduces with increasing time. This dip filling is found to be related to particle migration from regions of high shear rate to regions of low shear rate. No migration is observed below a concentration of 0.22. However, at these low concentrations, secondary currents may affect migration. The migration phenomenon is analysed within the framework of a two-phase model in which the particle migration flux is related to the divergence of the particle-phase stress (see e.g. Nott & Brady 1994; Morris & Boulay 1999). Since the particle-phase stress cannot be inferred directly from the experiments, a phenomenological form is assumed and tested against the experimental data (Morris & Boulay 1999). Good quantitative agreement is obtained when the normal stresses of the particle phase are set identical to the previously measured normal stresses of the whole suspension.

https://doi.org/10.1017/jfm.2011.272 Published online by Cambridge University Press

The origin of the particle-phase stress is still a subject of debate. However, one can assume that it contains two parts: a non-hydrodynamic contact stress which comes from the direct contacts between the particles and a hydrodynamic stress which arises solely from the hydrodynamic interactions between the particles. The original suspension balance model (Nott & Brady 1994; Morris & Boulay 1999) equated this latter hydrodynamic part to the contribution of the (bulk) suspension stress resulting from the dispersed particles, i.e. the hydrodynamic part coming from the stresslet contribution (Batchelor & Green 1972). However, the assumption that this particle contribution to the (bulk) suspension stress is responsible for migration has been questioned recently as this contribution is not present in the particle-phase momentum equation of the classical two-phase models (Lhuillier 2009; Nott *et al.* 2011). The origin of migration in this revisited suspension balance lies either in the non-hydrodynamic contact stress or in the non-drag part of the inter-phase force which can be written as the divergence of a hydrodynamic stress (Nott *et al.* 2011). This latter hydrodynamic part of the particle-phase stress is still connected to the suspension flow-induced structure and thus to the rheology but in a different way than thought initially. More precisely, it differs from the stresslet contribution and does not contribute to the stress of the whole suspension. In other words, only the contact stress is part of both the stress of the bulk suspension and that of the particle phase. This is the major difference between the original (Nott & Brady 1994; Morris & Boulay 1999) and revisited (Lhuillier 2009; Nott *et al.* 2011) models. Consequently, if the revisited model were to be adopted, the fact that using the normal stresses of the bulk suspension is sufficient to rationalize the migration observations would suggest that contact stress prevails (i) in the particle-phase stress and thus in the migration process and (ii) in the normal stress difference of the whole suspension above a volume fraction of 0.22.

Funding from Agence Nationale de la Recherche (Project RSC ANR-08-BLAN-0048-CSD2) and the Indo-French Centre for the Promotion of Advanced Research (IFCPAR Project Number 3404-1) is gratefully acknowledged.

REFERENCES

ABOTT, J. R., TETLOW, N. & GRAHAM, A. L. 1991 Experimental observations of particle migration in concentrated suspensions: Couette flow. *J. Rheol.* **35**, 773–795.

BARNES, H. A. 1995 A review of the slip (wall depletion) of polymer solutions, emulsions and particle suspensions in viscometers: its cause, character, and cure. *J. Non-Newtonian Fluid Mech.* **56**, 221–251.

BATCHELOR, G. K. & GREEN, J. T. 1972 The determination of the bulk stress in a suspension of spherical particles to order c2. *J. Fluid Mech.* **56**, 401–427.

BEAVERS, G. S. & JOSEPH, D. D. 1975 The rotating-rod viscometer. *J. Fluid Mech.* **69**, 475–512.

COUTURIER, É., BOYER, F., POULIQUEN, O. & GUAZZELLI, É. 2011 Suspensions in a tilted trough: second normal stress difference. *J. Fluid Mech.* 10.1017/jfm.2011.315.

DE GENNES, P.-G. 1979 Conjectures on the transition from Poiseuille to plug flow in suspensions. *J. Phys. France* **40**, 783–787.

GADALA-MARIA, F. & ACRIVOS, A. 1980 Shear-induced structure in a concentrated suspension of solid spheres. *J. Rheol.* **24**, 799.

EINSTEIN, A. 1905 Über die von der molekularkinetischen Theorie der Wärme geforderte Bewegung von in ruhenden Flüssigkeiten suspendierten Teilchen. *Ann. Phys.* (4) **17**, 549–560 1956, reprinted in *Investigations on the Theory of Brownian Movement*. Dover Publications.

KRIEGER, I. M. 1963 A dimensional approach to colloid rheology. *Trans. Soc. Rheol.* **7**, 101–109.

https://doi.org/10.1017/jfm.2011.272 Published online by Cambridge University Press

KRIEGER, I. M. 1972 Rheology of monodisperse lattice. *Adv. Colloid Interface Sci.* **3**, 111–136.

LEIGHTON, D. T. & ACRIVOS, A. 1987 The shear-induced migration of particles in concentrated suspensions. *J. Fluid Mech.* **181**, 415–439.

LHUILLIER, D. 2009 Migration of rigid particles in non-Brownian viscous suspensions. *Phys. Fluids* **21**, 023302.

MORRIS, J. F. & BOULAY, F. 1999 Curvilinear flows of noncolloidal suspensions: the role of normal stresses. *J. Rheol.* **43**, 1213–1237.

MORRIS, J. F. 2009 A review of microstructure in concentrated suspensions and its implication for rheology and bulk flow. *Rheol. Acta* **48**, 909–923.

NIR, A. & ACRIVOS, A. 1973 On the creeping motion of two arbitrary-sized touching spheres in a linear shear field. *J. Fluid Mech.* **59**, 209–223.

NOTT, P. R. & BRADY, J. F. 1994 Pressure-driven flow of suspensions: simulation and theory. *J. Fluid Mech.* **275**, 157–199.

NOTT, P. R., GUAZZELLI, É. & POULIQUEN, O. 2011 The suspension balance revisited. *Phys. Fluids* **23**, 043304.

OVARLEZ, G., BERTRAND, F. & RODTS, S. 2006 Local determination of the constitutive law of a dense suspension of non-colloidal particles through MRI. *J. Rheol.* **50**, 259–292.

RICHARDSON, J. F. & ZAKI, W. N. 1954 Sedimentation and fluidization: part I. *Trans. Inst. Chem. Engrs* **32**, 35–53.

SIEROU, A. & BRADY, J. F. 2002 Rheology and microstructure in concentrated non-colloidal suspensions. *J. Rheol.* **46**, 1031–1056.

SINGH, A. & NOTT, P. R. 2000 Normal stresses and microstructure in bounded sheared suspensions via Stokesian dynamics simulations. *J. Fluid Mech.* **412**, 279–301.

SINGH, A. & NOTT, P. R. 2003 Experimental measurements of the normal stresses in sheared Stokesian suspensions. *J. Fluid Mech.* **490**, 293–320.

STICKEL, J. J. & POWELL, R. L. 2005 Fluid mechanics and rheology of dense suspensions. *Annu. Rev. Fluid Mech.* **37**, 129–149.

TAYLOR, G. I. 1923 Stability of a viscous liquid contained between two rotating cylinders. *Phil. Trans. R. Soc. Lond.* A **223**, 289–343.

TAYLOR, J. R. 1982 An introduction to error analysis. In *University Science Books*. Oxford University Press.

TETLOW, N. *et al*. 1998 Particle migration in a Couette apparatus: experiment and modeling. *J. Rheol.* **42**, 307–328.

WILSON, H. J. 2005 An analytic form for the pair distribution function and rheology of a dilute suspension of rough spheres in plane strain flow. *J. Fluid Mech.* **534**, 97–114.

ZARRAGA, I. E., HILL, D. A. & LEIGHTON, D. T. 2000 The characterization of the total stress of concentrated suspensions of noncolloidal spheres in Newtonian fluids. *J. Rheol.* **44**, 185–220.

https://doi.org/10.1017/jfm.2011.272 Published online by Cambridge University Press